Advances in Differential Equations and Control Processes 2026, 33(3), 4621.
doi: https://doi.org/10.59400/adecp4621

Article

Rainfall-induced instability mechanism of high-altitude gravelly soil slopes and machine learning surrogate modeling

Jianli Jin[1,2,3,*], Yuhao Zheng[1,2], Yongchen Zong[1,2], Baoliang Wang[4], Qiang He[1,2,3]

[1] College of Water Conservancy and Civil Engineering, Xizang Agricultural and Animal Husbandry University, Linzhi 860000, China; 123456zyh@163.com (Yuhao Zheng); zongyongchen@xza.edu.cn (Yongchen Zong); heqiang@xza.edu.cn (QH)
[2] Research Center of Civil, Hydraulic and Power Engineering of Xizang, Xizang Agricultural and Animal Husbandry University, Linzhi 860000, China
[3] Key Laboratory of Transport Industry of Wind Resistant Technology for Bridge Structures, Tongji University, Shanghai 200092, China
[4] Nuclear Industry Southwest Geotechnical Investigation & Design Institute Co., Ltd., Chengdu 610052, China; xzdnjs@163.com
*** Corresponding authors:** Jianli Jin, jljin@xza.edu.cn

CITATION

Jin J, Zheng Y, Zong Y, et al. Rainfall-induced instability mechanism of high-altitude gravelly soil slopes and machine learning surrogate modeling. Advances in Differential Equations and Control Processes. 2026; 33(3): 4621. https://doi.org/10.59400/adecp4621

ARTICLE INFO

Received: 5 July 2026
Revised: 19 August 2026
Accepted: 24 August 2026
Available online: 28 August 2026

Abstract: This study investigates the distinctive instability mechanism of high-altitude gravelly-soil slopes driven by particle gradation, weak clayey characteristics and intense rainfall. Soil parameters were obtained from laboratory tests on a typical high-steep bedding gravelly-soil slope in the Parlung Zangbo Basin, southeastern Tibet. A fully coupled stress-pore-pressure finite-element model was built in ABAQUS to simulate seepage-deformation responses under six rainfall intensities and multiple durations. An infiltration threshold of 1.9×10^{-4} cm/s is determined. This threshold, a near-surface transient saturated zone, develops rapidly and impedes infiltration. Pore-water-pressure at the slope toe responds roughly 12 h earlier than at the crest. Every 10 cm increase in cumulative infiltration produces approximately 15 mm extra toe horizontal displacement ($R^2 = 0.93$, 95% confidence interval (CI): 1.43–1.61). A 32-h deformation lag is observed post-rainfall, representing the period required for displacement to attain 90% of its stable value. Random-forest surrogate models for toe displacement and pore-water pressure are trained on 1,296 spatiotemporal finite-element samples, yielding test-set $R^2 > 0.96$. Comparisons with Gaussian process regression, support vector regression and eXtreme Gradient Boosting (XGBoost) reveal that XGBoost achieves optimal accuracy (horizontal-displacement root mean square error (RMSE) = 0.42 mm), while random forest provides competitive performance (mean absolute percentage error (MAPE) = 7.8%) and better interpretability. A classification model detects transient saturated zones at 92.3% accuracy. This coupled numerical-simulation and machine-learning framework provides a new tool for rapid early-warning and parameter-sensitivity analysis of similar high-altitude rainfall-induced slope hazards.

Keywords: high-altitude cold region slope; gravelly soil; rainfall-induced instability; fully coupled analysis; transient saturated zone; machine learning surrogate model

1. Introduction

The Tibetan Plateau, which exceeds 4,000 m in average height, is characterized by high solar radiation, large day and night temperature differences, and annual freeze-thaw cycles occurring annually across most of it. In southeast Tibet, warm, humid air from the Indian Ocean strongly influences the Palongzangbu River basin, which receives more than 1,600 mm of rainfall annually from May to October. As a result, the effects of river erosion and sediment transport are very active, and a valley landscape has been formed typical of the alpine zone [1–4]. The regional geological structure is complex, strata intensely dissected by weak-weathering resistance granite, gneiss, and argillaceous slate rock mass. Thick weathered and loose deposits have formed due to cold climate weathering. These deposits exhibit poor gradation and a minor clay fraction (about 2.03% of particles <0.005 mm), forming a unique high-altitude gravelly soil slope. Low-temperature sliding slopes are specific types of earth materials that are representative of China and the world because their geotechnical structure, hydraulic response and deformation-failure mechanism are fundamentally different from low-elevation slopes [5–8].

Research on plateau permafrost is relatively mature, and the instability mechanism of high-altitude coarse-grained soil slopes induced by rainfall has become a new research focus [9]. Several research results show that freeze-thaw cycles can considerably alter the pore structure and mechanical characteristics of coarse-grained soil. Furthermore, substantial alterations are observed in the permeability of these soils; fine particle content and freeze-thaw frequency exert a joint effect on permeability [10, 11]. Besides, temperature can significantly impact the strength and deformation characteristics of coarse-grained soil [12, 13]. In slopes with frozen soil, creep sliding, surficial collapse and shallow sliding can often occur in winter. Meanwhile, the failure zone (or shear surface) increasingly extends to deeper and deeper positions when freeze–thaw and rainfall work together. At high altitudes, coarse-grained soils are commonly subjected to prolonged low temperature weathering and infiltration from rain and snowmelt. So, the mechanical and seepage properties of high-altitude coarse-grained soils are usually not the same as those of ordinary soils [14, 15].

Regional slope stability analysis has been done in detail. Statistical raindrop thresholds imply that landslides tend to occur when the daily rainfall has crossed 45 mm [16, 17]. Researchers have used digital elevation model (DEM) interpretation and field work for characterizing failure pattern and spatial distribution of landslides in southeaster Tibet [18]. Model tests and classical numerical simulations have been undertaken to understand slope failure machanism [19, 20], and causes analysis and risk prediction has been done using historical disaster catalogue data [21, 22]. In the last few years, machine learning methods have seen increasing application in slope stability analysis, deviating from historical limit equilibrium and numerical simulation towards a combination of data-driven and physics-based approaches [23, 24].

The shortcomings, which are the starting point and the innovations of this study have been highlighted in the literature.

There are no fully coupled analyses of high-altitude gravelly soil slopes that are quantitative in nature. Most analyses on rainfall infiltration takes either seepage or stress as only physical field. The synergistic control of seepage and deformation is due to a unique gradation and lesser clay content of high-altitude soils.

The transient saturated zone and the disaster-mitigation function of hydraulic barriers remain unquantified. A majority of the existing studies which have been conducted for evaluating landslide susceptibility are primarily qualitative in nature. They fail to take into consideration the unique hydrological response of high-altitude gravelly soils. These soils respond in this manner primarily due to their high permeability and pronounced unsaturated characteristics.

No numerical simulation methods have been adapted for high-altitude coarse-grained soils, thus lacking rapid prediction tools. The computation time required for a single finite element is 2–4 h, which unduly compromises real-time early warning and parameter sensitivity analysis tasks.

To mitigate the above issues, the present study attempts to examine a typical high-steep, consequent gravelly soil slope at K4056+300. It is located within the Palongzangbu River basin, Linzhi, Tibet. We carried out systematic laboratory tests of the soil. This was done keeping in view the poor gradation and weak clay of high-altitude coarse-grained soil. Using the fully coupled stress–pore-pressure finite element model in ABAQUS, we designed scenarios of multiple rainfall intensities (0.2–20 mm/h) and durations. Using 1,296 spatiotemporal samples produced by finite element calculations, a random forest surrogate model was developed for the second-scale prediction of slope responses. A collaborative approach of "fully coupled numerical simulation + machine learning surrogate model" developed in this paper provides model support for rapid early warning of rainfall-induced disasters on high-steep slopes along Sichuan-Tibet highway.

2. Engineering overview

2.1. Geological structure and regional background

Palongzangbu River basin is part of Yigongzangbu-Palongzangbu river system. The Nyainqentanglha Mountains, the Himalayas, the Gangdise Mountains, and the Yarlung Zangbo River fault zone jointly control it. The geological structure of the region is very complicated, with high spatial variability of lithology, topography, and geomorphology. The area experiences geological hazards that are manifold, large-scale and extremely sudden. The operations of trunk highways, national defense security, and the health and safety of local residents and their property suffer serious effects from a chain reaction of high-altitude snowfall and freeze-thaw.

2.2. Landslide geometric characteristics

The slope under investigation is situated on the right-hand side of the Yigongzangbu River by the YigongTongmai highway. The slope is long, strip-shaped, with a slope aspect of 45°, an overall slope angle of about 40°, and planar slope surface. The toe elevation stands at 2,094 m, the crest elevation at 2,694 m, and the slope height at 600 m. The width of the model, which is perpendicular to slope aspect, is 30 m. The loose deposit (slope surface) has a total area of about 21,600 m^2 and a total volume of about 1.08×10^5 m^3 (according to the average thickness of 5 m). It is indicative of a classic steep and high slope.

2.3. Stratigraphic lithology and hydro-meteorological conditions

The base rock of the slope consists of gneiss from the Nyainqentanglha Group, which is covered by glaciofluvial loose deposits. The majority of regional surface water comes from rainfall in the atmosphere, and winter snowpack and spring snowmelt continually recharge slope groundwater. Annual precipitation is about 1,000 mm a year. The shear strength and overall stability of the loose deposit is significantly decreased by the combined infiltration of ample rain and meltwater. According to **Figure 1**, Linzhi City experiences a mix of warm and cold weather.

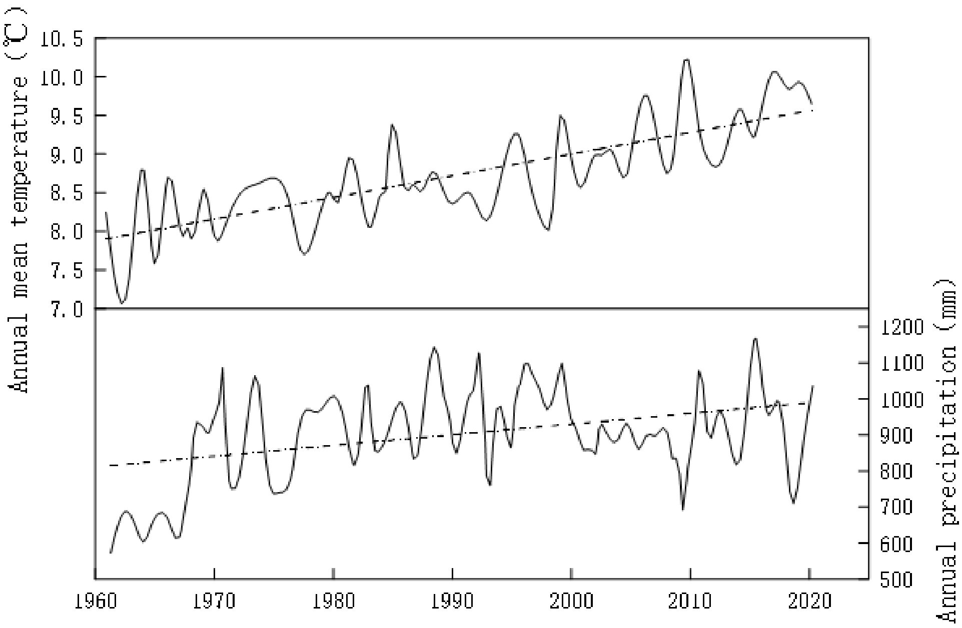

Figure 1. Annual average temperature and average rainfall in Linzhi City.

3. 3D numerical simulation of the landslide

3.1. Physical and mechanical parameter tests

Soil of high altitude slope was subjected to proper laboratory tests to find out its physical and mechanical parameters. Within the laboratory conditions, the authors executed large-scale triaxial tests using φ300 mm × 600 mm specimens, which allowed 60 mm particle sizes. The study was conducted at two relative densities, i.e., 0.6 and 0.9 and three confining pressures (0.3 MPa, 0.5 MPa, and 0.7 MPa) were established. The permeability, compaction and specific gravity tests were carried out using DLY−2 coarse−grained soil permeameter, multifunction electric compactor, and siphon pycnometer, respectively.

According to the grain size analysis, the d_{60} and d_{30} parameters of the soil are found to be 7.25 mm and 0.73 mm, respectively. Further, the d10 is obtained as 0.19 mm. Thus, the uniformity coefficient C_u = 38.2 and coefficient of curvature C_c = 0.39 shows that poorly graded gravelly soil is present. The particles of the soil are analysed; it is found that particles greater than 0.075 mm are comparable to 97.78%; gravel particles above 2 mm are comparable to 56.45%, and the fine fraction analysis shows that particles smaller than 0.005 mm clay are comparable to 2.03%, indicating weak clay cementation. This is an essential trait rendering high-altitude coarse-grained soil different from ordinary crushed stone soil. **Table 1** summarizes the soil physical and mechanical parameters, and **Figure 2** shows the sampling locations on the slope model and the grading curve.

Table 1. Physical parameters of soil body.

Soil layer Project	ρ_d (g/cm^3)	c (kPa)	φ (°)	E (kPa)	μ	K (cm/s)
Gravelly soil	2.05	50.4	23.64	200,000	0.3	1.9×10^{-4}
Gneiss	2.75	300	40	800,000	0.36	2.0×10^{-5}
bedrock	3.00	800	45	1,000,000	0.36	2.0×10^{-7}

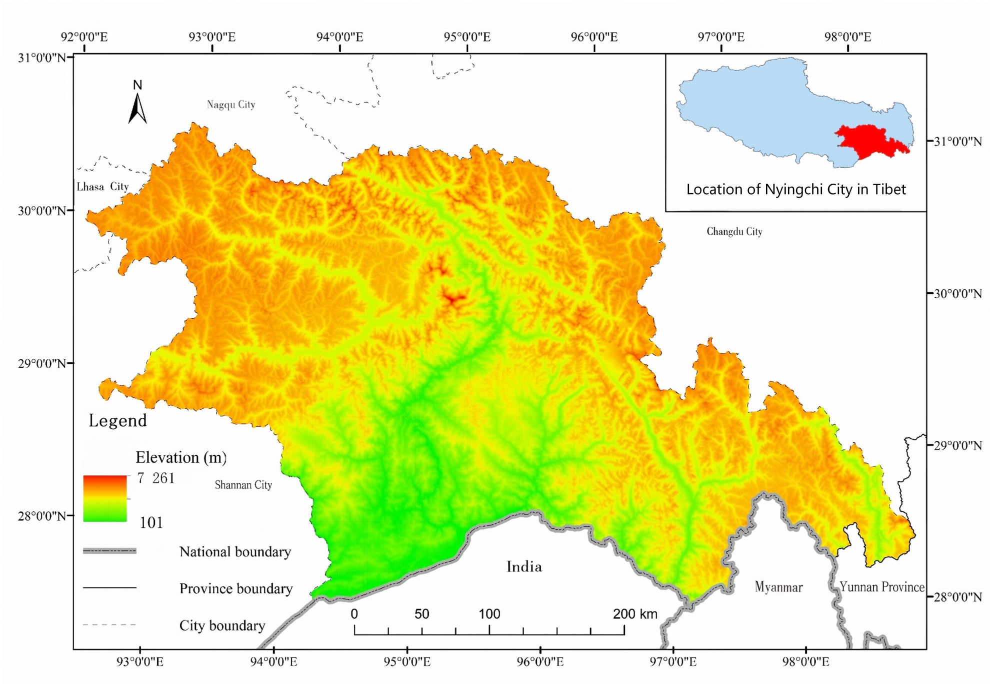

Figure 2. Sampling locations.

The relative permeability coefficient is calculated using the van Genuchten–Mualem model:

$$k_r = \sqrt{S_e}\left[1 - \left(1 - S_e^{1/m}\right)^m\right]^2 \tag{1}$$

where S_e is the effective degree of saturation, and $m = 1 - 1/n$.

3.2. Finite element model design

The geometry, material zoning and boundary conditions of the numerical model are illustrated in **Figure 3**, where gravelly soil overlies gneiss bedrock and the slope surface dips at 27° (upper segment) and 46° (lower segment). According to Richards' equation, unsaturated seepage was implemented, while soil was going to serve as a material within the Mohr–Coulomb elastic—perfectly plastic constitutive law. After pursuing a fully coupled stress–pore pressure approach, it resulted in simultaneous computation of the seepage and stress fields. The numerical solution utilizes automatic time stepping with a maximum of 15 iterations per increment and a convergence criterion of 0.005.

Figure 3. Slope.

Displacement constraint refers to the horizontal and vertical restraints of face AB and also restrained horizontally for face AF. The slope surfaces HE, EF and CH are taken as free displacement boundaries.

The face AB at the bottom is assigned a no flow boundary condition. The groundwater table has been assigned based on field measurements. The soil beneath the water table is completely saturated, whereas static pore water pressure above the water table varies linearly with depth as given by $u = \rho wg(100 - Y)$. In this equation, Y is the vertical height measured from bottom face AB.

The rainfall infiltration boundary condition is applied to slope surfaces FE, ED, and DC. Surface AB is impervious.

3.3. Rainfall scenario design

From May to September, the Palongzangbu River basin experiences its most rainy season. 90% of the yearly rainfall occurs in this period. According to the national meteorological rainfall grading standard, six rainfall intensity and several combinations of rainfall and rainfall-stop durations have been established, such as light rain (0.2 mm/h), moderate rain (1 mm/h), heavy rain (2 mm/h), downpour (4 mm/h), cloudburst (10 mm/h) and extreme cloudburst (20 mm/h). The three scenario types we designed were continuous rainfall, rainfall with a rain stop period, and long duration rainfall. The rainfall duration was kept uniform at 12 h for heavy rainfall intensities (≥4 mm/h). The rainfall scenarios are summarized above.

3.4. Governing equations and coupling method

Within the ABAQUS Soils analysis step, we relied on a fully coupled stress–pore pressure analysis module to resolve the stress field and transient seepage field concurrently. The seepage equation (Richards' equation), mechanical equilibrium equation, constitutive yield criterion (Mohr-Coulomb), and unsaturated characteristic functions (van Genuchten Mualem) are governing equations. The automatic time stepping for numerical solution is performed with a maximum of 15 iteration per increment and a convergence limit of 0.005 for the coupled calculation.

3.4.1. Seepage governing equation

The movement of water in unsaturated soil is governed by Richards' equation, where it is assumed that the gas phase is continuous and flow follows Darcy's law.

$$\frac{\partial}{\partial x}\left(k_x\frac{\partial h}{\partial x}\right)+\frac{\partial}{\partial y}\left(k_y\frac{\partial h}{\partial y}\right)+\frac{\partial}{\partial z}\left(k_z\frac{\partial h}{\partial z}\right)=m_w\rho_w g\frac{\partial h}{\partial t} \tag{2}$$

Where h is the total head (m), k_x, k_y, k_z are the anisotropic permeability coefficients (m/s), m_w is the slope of the soil-water characteristic curve (1/Pa), ρ_w is the density of water (kg/m^3), g is the acceleration due to gravity (m/s^2), and t is time (s).

3.4.2. Mechanical equilibrium equation

The equilibrium equation is grounded in the principle of virtual work. Water pressure in the pores is introduced in the stress field as equivalent nodal forces for hydraulic-mechanical two-way coupling. The Newton–Raphson iteration method updates simultaneously the displacement and pore pressure degrees of freedom, accommodating the high-altitude slope's complex medium characteristics.

3.4.3. Constitutive model and yield criterion

The Mohr–Coulomb (MC) model is used here because it has limited parameters and is widely used in engineering; moreover, it can reasonably describe the overall shear failure surface of the slope. The limits of it are mentioned in Section 6.6.

3.4.4. Unsaturated characteristic functions

The soil-water characteristic curve of the gravelly soil is shown in **Figure 4**, and the van Genuchten parameters were fitted as a = 0.05 kPa^{-1} and n = 1.5. The van Genuchten model defines the relationship between effective degree of saturation and matric suction and the relative permeability coefficient that varies non-linearly with saturation. The fitting parameters used for matching were a = 0.05 kPa^{-1} and n = 1.5. They match the coarse-grained soil of high altitude in the study area. Laboratory constant-head tests were utilized to determine the saturated permeability coefficient (**Table 1**).

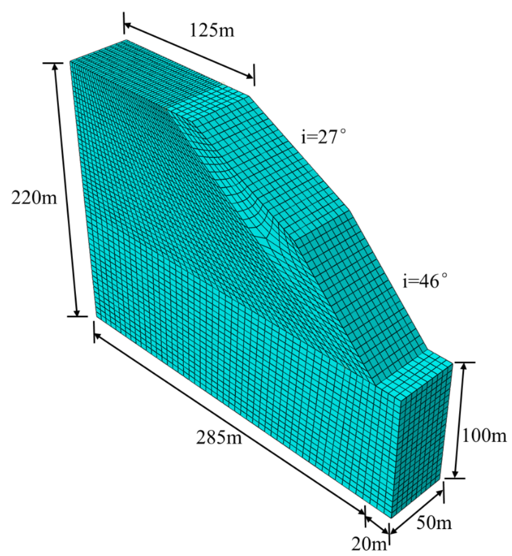

Figure 4. Model.

3.4.5. Coupling mechanism

Fluid pressure is introduced at each incremental step into the mechanical equilibrium equation. Also, volumetric strain caused by mechanical deformation re-acts on pore water pressure. Thus, Biot's two-way fully coupled formulation is achieved.

4. Response prediction based on machine learning and transient saturated zone identification

By utilizing a fully coupled numerical simulation and machine learning surrogate models, code direction for slope reliability analysis will be offered. In line with this concept, the current study integrates fully coupled finite element computation with a random forest surrogate model.

4.1. Sample collection

As can be seen from **Figure 5**, the overall technical roadmap consists of numerical-simulation sampling, data preprocessing, surrogate-model construction, evaluation and physical-consistency verification. The technical workflow in this paper, which is a complete technical workflow, includes the following stages: numerical simulation sampling, data preprocessing, dataset division, surrogate model construction, hyperparameter optimization, prediction and classification evaluation, interpretability analysis, physical consistency verification, and engineering threshold extension. We, first of all, utilized ABAQUS for multi-scenario calculation to extract spatiotemporal monitoring samples. Following the removal of outliers, investigation of feature correlation, and standardization of data, we applied Time-series Stratified sampling to split the data into Training, Validation, and Test datasets. Random forest was used to develop regression and classification model and hyper-parameter tuning was done through grid search. The overall technical roadmap can be seen from **Figure 6**. See **Figure 7** for computational workflow.

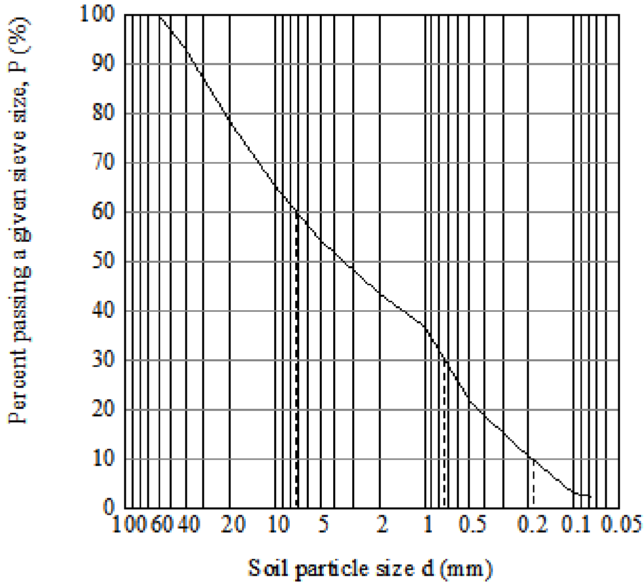

Figure 5. Grading curves.

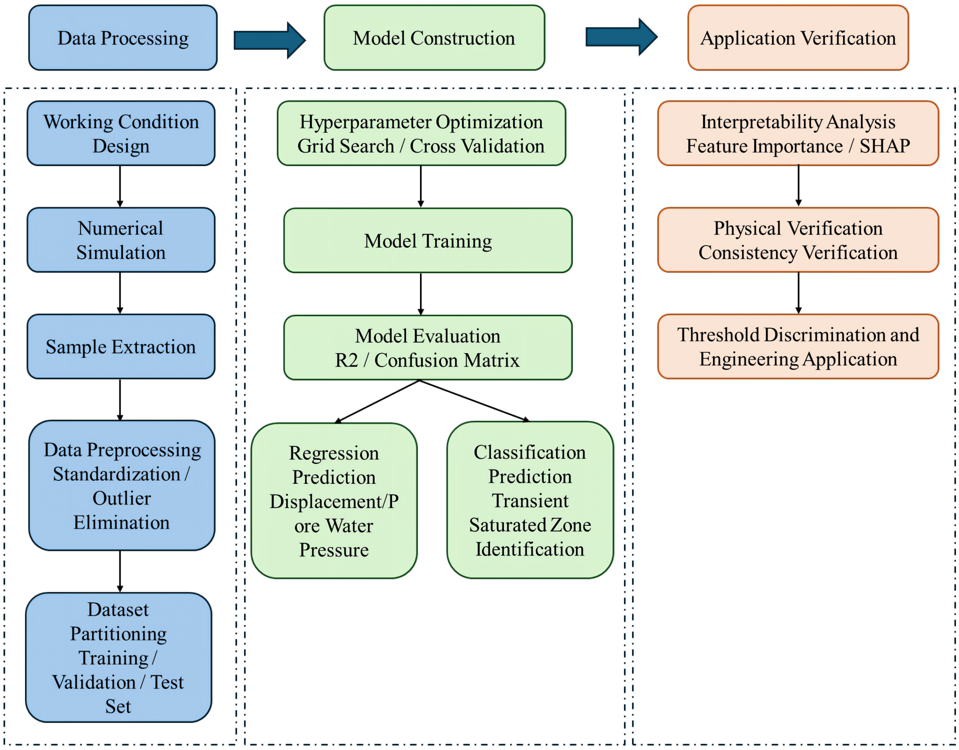

Figure 6. Overall technical route of machine learning.

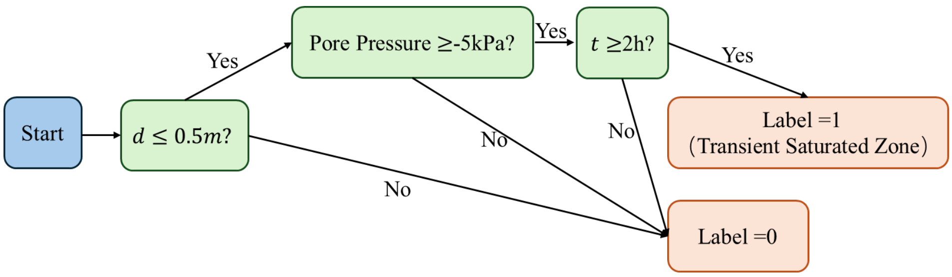

Figure 7. Flowchart.

4.2. Dataset construction and data preprocessing

4.2.1. Sample collection

Samples were extracted from ABAQUS simulation outputs, covering data for all 12 rainfall-cessation scenarios listed in **Table 2**. Three monitoring cross-sections were set at the slope crest, mid-slope, and slope toe. Three monitoring depths (surface, 0.5 m, and 1.0 m) were assigned to each cross-section, yielding a total of 9 spatial monitoring points. For each scenario, 12 time instants were evenly sampled at a 2-h interval across the valid simulation period. These sampled time points cover the complete physical process of rainfall infiltration and post-rain pore-water-pressure dissipation. The total sample size is calculated as: 12 scenarios × 12 time instants × 9 monitoring points = 1,296 datasets.

4.2.2. Input features and output labels

To construct the machine learning surrogate model, the input features and output targets of the model need to be clearly defined. In this study, considering rainfall conditions, spatial location, and rainfall cessation status, seven key physical quantities were selected as input features, while the horizontal displacement at the slope toe and pore water pressure were taken as the regression output labels. The specific definitions are presented in **Table 3**.

Table 2. Design scheme of rainfall intensity and rainfall duration.

Rainfall intensity	**Light rain**	**Moderate rain**	**Heavy rain**	**Torrential rain**	**Very heavy rain**	**Extreme rainfall**
Rainfall	0.2 mm/h	1 mm/h	2 mm/h	4 mm/h	10 mm/h	20 mm/h
Rainfall conditions	Rainfall 96 h (96–0.2) Rainfall 96 h, Rain cessation 96 h (96–96–0.2) Rainfall 192 h (192–0.2)	Rainfall 96 h (96–1) Rainfall 96 h, Rain cessation 96 h (96–96–1) Rainfall 192 h (192–1)	Rainfall 96 h (96–2) Rainfall 96 h, Rain cessation 96 h (96–96–2) Rainfall 192 h (192–2)	Rainfall 12 h (12–4)	Rainfall 12 h (12–10)	Rainfall 12 h (12–20)

Table 3. Input features and regression output labels of the model.

Category	**Feature/tag name**	**Symbol**	**Unit**	**Remarks**
Input features	Rainfall intensity	I	mm/h	—
	Cumulative rainfall	P_{cum}	mm	—
	Rainfall duration	t	h	—
	Relative elevation of monitoring points	H_{rel}	m	Relative toe of slope
	Depth from the slope surface	d	m	0 = Surface layer
	Rain stop status indicator	—	—	0 = Raining, 1 = Rain
	Rain stop duration	t_{dry}	h	Valid when raining stops
Regression label	Horizontal displacement	—	mm	Slope toe monitoring point
	Pore water pressure	—	kPa	—

Furthermore, to enable rapid identification of the transient saturated zone, a binary classification criterion was established based on the physical laws revealed by numerical simulations (surface layer depth ≤ 0.5 m, pore water pressure ≥ −5 kPa, rainfall duration ≥ 2 h). Samples satisfying all of the above conditions were labeled as the transient saturated zone; otherwise, they were classified as the non-transient saturated zone. The detailed classification criteria are shown in **Table 4**.

Table 4. Criterion for binary classification label of transient saturated zone.

Judgment criteria (must be satisfied simultaneously)	**Classification tag**
Depth from the slope surface $d \leq 0.5$ m Pore water pressure is greater than or equal to −5 kPa Rainfall duration $t \geq 2$ h	1 (Transient Saturated Zone)
Any of the above conditions are not met	0 (Non-transient Saturated Zone)

Note: The threshold is comprehensively determined based on the soil permeability characteristics of the study area (saturated hydraulic conductivity 1.9×10^{-4} cm/s) and existing research on cold-region slopes. For the binary classification task of transient-saturated-zone identification, the dataset contains 391 samples labeled as 1 (transient saturated zone) and 905 samples labeled as 0 (non-transient saturated zone).

4.2.3. Data preprocessing

Our float measurement campaign involved using box plots alongside the 3σ criterion to eliminate simulated anomalous outliers, allowing us to reliably extract underlying geophysical signals. In order to eliminate dimensional differences between the features and enable multi-model comparison and interpretability analysis, the features were standardized using Z-score standardization. For testing feature multicollinearity, we created correlation heatmaps and checked the variance inflation factor (VIF) to keep physically dominant features while ensuring an independent input.

With the help of temporal stratified sampling, the entire dataset was divided at the ratio of 70–15–15 into the training set, validation set, and test set, respectively. This careful avoidance of data leakage ensured that the generalization evaluation is authentic and reliable.

4.3. Random forest model and training setup

The Bagging ensemble learning framework uses random forest, which employs decision trees for base learners. The model was built in Python 3.9 using Scikit-learn. We executed a hyperparameter optimization using grid search with 5-fold cross-validation. The optimal parameters are found to be number of decision trees = 200, maximum depth of tree = 15, and minimum number of samples in leaf = 5.

4.4. Model performance evaluation

As shown in **Table 5**, we present the whole set of evaluation metrics for the models. With the regression tasks, we include mean absolute error (MAE) and mean absolute percentage error (MAPE). With classification tasks, we included precision, recall, F1-score, area under the curve (AUC) and confusion matrix.

Table 5. Model evaluation results.

Task	Model	Evaluation metrics	Test set results
Horizontal Displacement Prediction	Random Forest Regression	R^2	0.964
		RMSE	1.27 mm
Pore Water Pressure Prediction	Random Forest Regression	R^2	0.971
		RMSE	2.54 kPa
Transient Saturated Zone Identification	Random Forest Classification	Accuracy	92.3%

The random forest model performance on the testing set for predicting the pore water pressure and horizontal displacement is shown in **Figure 8**. The paragraph suggests that the predicted points of pore water pressure and horizontal displacement both cluster close to the 45° diagonal line without any evident systematic bias. The random distributions of residuals around the zero lines for pore water pressure and displacement indicate that both the residuals show no obvious heteroscedasticity or trend bias, further verifying the model's stability and unbiasedness. **Figure 9** compares the predicted and simulated pore-water pressure and horizontal displacement on the test set: the predicted points cluster along the 45° diagonal line without systematic bias, and the residuals are randomly distributed around zero, indicating stable and unbiased model performance.

4.5. Feature importance analysis

Table 6 shows the ranking of feature importance (mean decrease in impurity) as provided by random forest. The results suggest that cumulative rainfall is the most important feature, which aligns with the physical law "cumulative infiltration controls deformation magnitude". Depth and elevation highlight that the shallow layer near the slope toe is a high-risk area for instability.

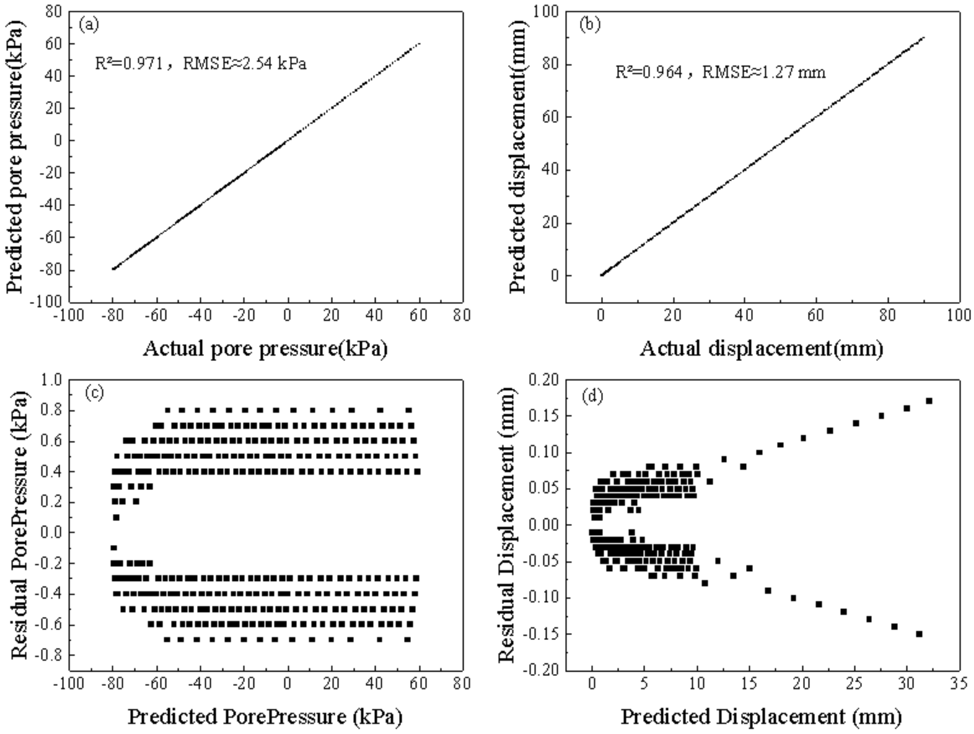

Figure 8. **(a)** Pore water pressure prediction result; **(b)** Displacement prediction result; **(c)** Residual distribution of pore water pressure; **(d)** Residual distribution of displacement.

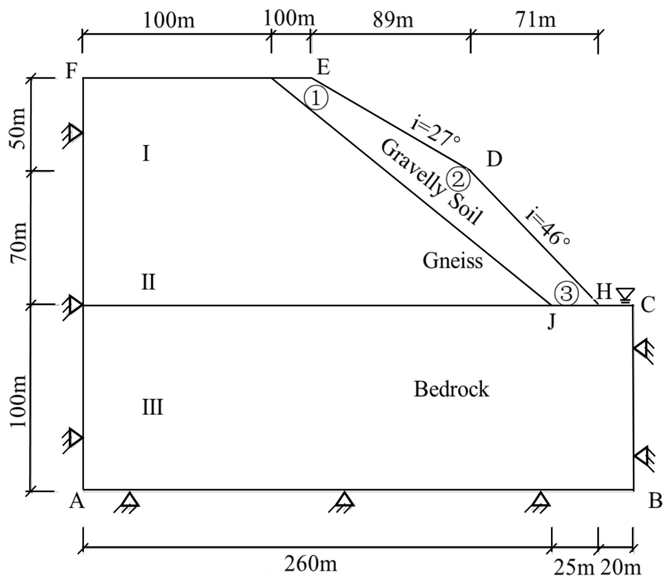

Figure 9. Soil water characteristic curve [25].

Table 6. Feature importance ranking (for displacement prediction).

Ranking	Feature	Importance score
1	Cumulative rainfall	0.342
2	Depth from the slope surface	0.219
3	Relative elevation	0.187
4	Rain stop duration	0.109
5	Rainfall intensity	0.078
6	Rainfall duration	0.047
7	Rain stop stage sign	0.018

4.6. Multi-dimensional threshold discrimination for transient saturated zone formation

Finite element analysis indicates a single infiltration threshold of 1.9×10^{-4} cm/s. However, the actual infiltration threshold has a dynamic relationship with the initial water content and matric suction. When the initial matric suction is 60 kPa, the random forest classification model extends the fixed threshold to a multi-dimensional discriminant surface; the critical rainfall intensity increases to 2.3×10^{-4} cm/s; when the initial matric suction is 20 kPa, the critical rainfall intensity decreases to 1.5×10^{-4} cm/s. The threshold model can effectively determine early warning thresholds for field slopes dynamically.

4.7. Performance comparison and selection basis of different machine learning models

To evaluate the relative performance of the four machine learning models on the slope dataset, we compared Random Forest (RF), Gaussian Process Regression (GPR), Support Vector Regression (SVR), and eXtreme Gradient Boosting (XGBoost) in terms of their predictive accuracy for toe horizontal displacement and pore water pressure. The evaluation metrics included the coefficient of determination (R^2), root mean square error (RMSE), and mean absolute error (MAE). As shown in the bar chart of **Figure 10**, XGBoost achieves the best performance across all six metrics, with an R^2 of 0.9942 and an RMSE of 0.42 mm for displacement prediction, and an R^2 of 0.9988 and an RMSE of 0.97 kPa for pore water pressure prediction. SVR ranks second, with a displacement R^2 of 0.9709 and an RMSE of 0.94 mm. Although RF exhibits slightly lower accuracy than SVR (displacement $R^2 = 0.964$), its intrinsic feature importance analysis capability provides a unique advantage in model interpretability, which is of practical value in engineering early-warning applications. GPR performs significantly worse than the other models on this dataset (displacement $R^2 = 0.158$), indicating that the standard kernel function fails to effectively capture the nonlinear characteristics of slope response; thus, it is not recommended for standalone use in such engineering predictions.

It is noteworthy that all models achieve higher prediction accuracy for pore water pressure than for displacement, which is consistent with the underlying physical mechanism—pore water pressure is directly governed by Richards' equation, whereas displacement involves multi-step transmission through Biot coupling, leading to enhanced nonlinearity and greater prediction difficulty. Considering both prediction accuracy and interpretability requirements, Random Forest is selected as the core surrogate model in this study. It should be noted that although XGBoost delivers optimal prediction performance, its interpretability relies on additional SHapley Additive exPlanations (SHAP) toolkits. By contrast, Random Forest outputs built-in feature-importance results without extra post-processing, making it more feasible for practical engineering early-warning scenarios [26].

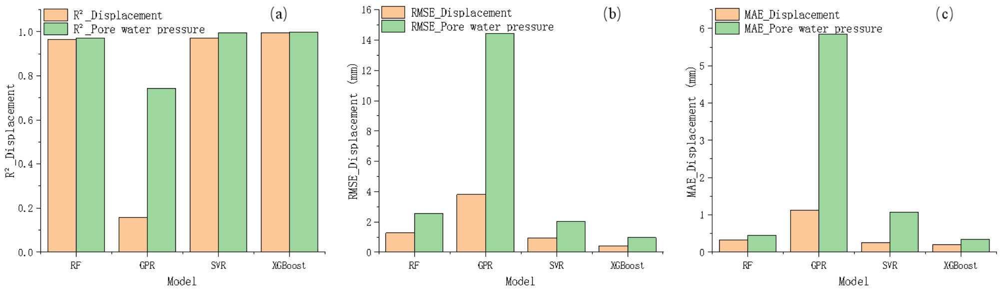

Figure 10. Prediction performance comparison of four machine-learning models (RF, GPR, SVR, XGBoost): **(a)** Horizontal displacement at the slope toe; **(b)** Pore-water pressure. Evaluation metrics include the coefficient of determination (R^2), root-mean-square error (RMSE), and **(c)** Mean absolute error (MAE).

5. Results

5.1. Analysis of pore water pressure characteristics

As told by **Figure 11**, the pore water pressure varied with time. During rainfall infiltration and post-rain dissipation, pore pressure at the crest slowly rises, whilst that at the toe is more sensitive. The response of pore pressure at the toe comes before that at the crest by about 12 h. Negative pore pressure (matric suction) is maintained under all scenarios. Based on the connection between rainfall intensity and soil permeability coefficient, there may be two response modes.

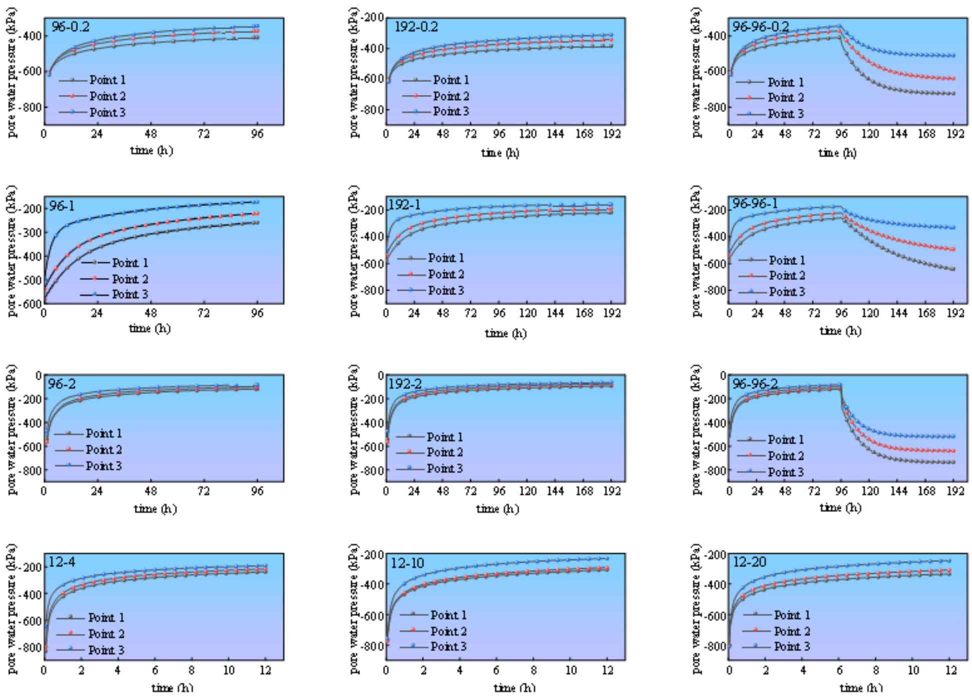

Figure 11. Trend diagram of pore water pressure over time.

1. The greater the rainfall intensity, the larger the infiltration amount will be and the faster will be the rise of pore pressure in case of rainfall intensity lower than the permeability coefficient of soil (0.2, 1, 2, 4 mm/h).
2. In case rainfall intensity is greater than the coefficient of permeability of soil (10, 20 mm/h), a transient saturated zone quickly builds up on the slope surface, which

acts as a hydraulic barrier and restricts deep infiltration. Consequently, pore-water pressure stabilises rapidly, and infiltration depth is limited.

5.2. Volumetric water content characteristics

Slope volumetric water content varies as shown in **Figure 12**. Overall volumetric water content increases due to rainfall, with the toe having a greater rate of increase than the crest. After the rainfall ends, the water content at the top decreases rapidly. However, the water content at the toe remains high for a long-time. Under low rainfall intensity, the macro-spaces will not fill up. The surface layer saturates quickly during short-duration heavy rainfall, preventing deep water recharge.

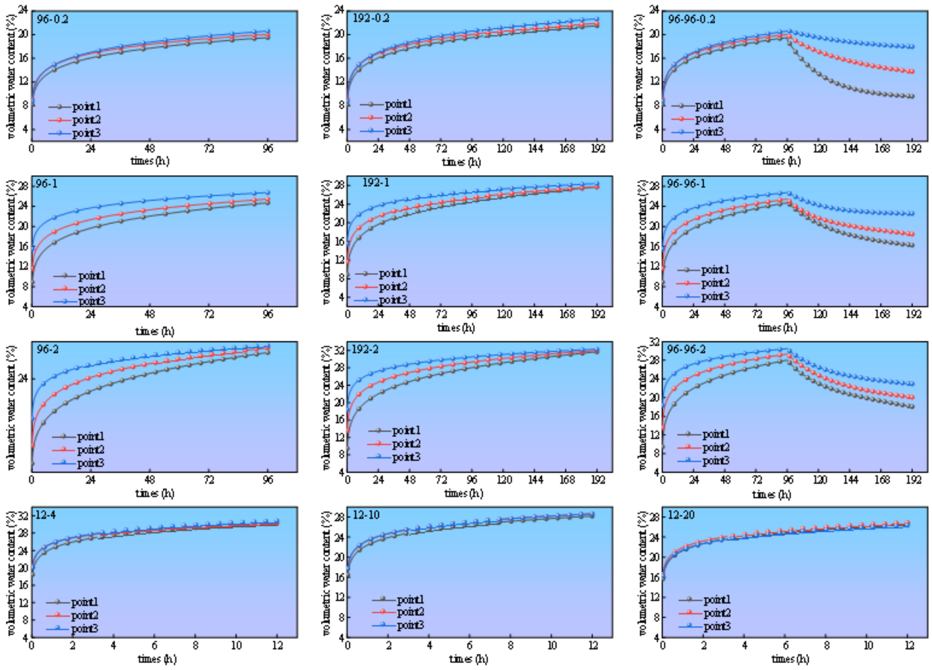

Figure 12. Variation diagram of volume water content.

5.3. Variation of seepage velocity

The seepage velocity at every monitoring point is represented in **Figure 13**, while **Figure 14** represents seepage velocities under various scenarios. On the whole, at the inception of rainfall, the seepage velocity is low; with continuous infiltration, the saturation of soil increases, the coefficient of unsaturated permeability increases and seepage velocity rises rapidly. When the rainfall intensity is low (1 mm/h), seepage velocity reaches a balance state within about 24 h, but when the rainfall intensity is high (2 mm/h), the saturation continues to rise and the seepage velocity shows a long-term increasing trend.

5.4. Horizontal displacement of the slope

The slope toe's horizontal displacement evolution is illustrated in **Figure 15**. Rain fall influence on deformation of slope moves from toe toward the crest progressively. A threshold effect of rainfall intensity has been observed, which results in the toe displacement increment becoming saturated when rainfall intensity was more than 10 mm/h. Under low to moderate rainfall intensities, deformation is largely dependent upon cumulative infiltration. After the rain stops, slope deformation has a lag of 32 h. As cumulative infiltration increases by 10 cm, the toe displacement is likely to increase by 15.2 mm. $R^2 = 0.93$, $p < 0.01$, n = 108, 95% CI: 1.43–1.61.

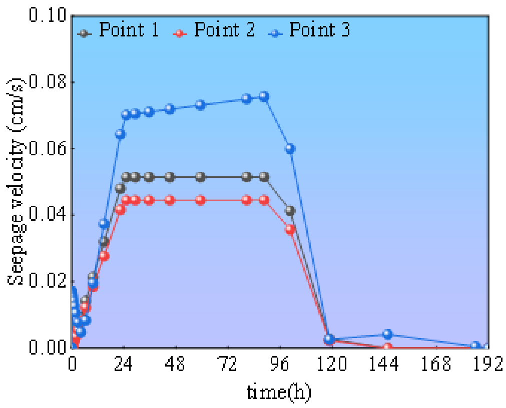

Figure 13. Seepage velocity at different elevations.

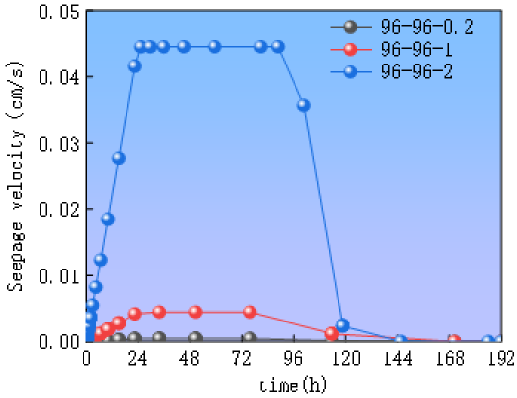

Figure 14. Seepage velocity under different rainfall intensities.

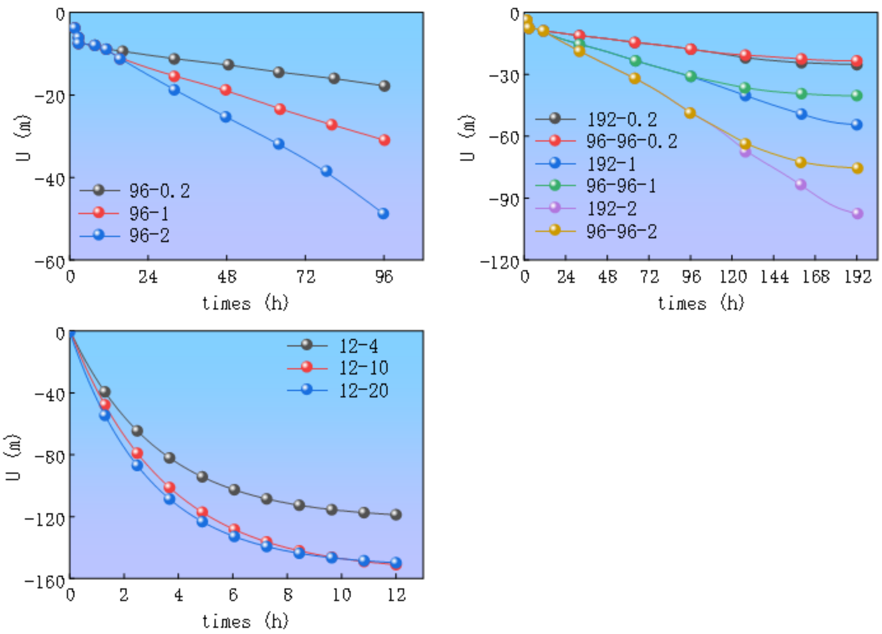

Figure 15. Horizontal displacement at the slope toe.

5.5. Study of equivalent plastic strain of the slope

As shown in **Figure 16**, the evolution of equivalent plastic strain at the toe of the slope. Heavy rainfall decreases matric suction and weakens interparticle cementation causing yields a development of plastic strain. Under the high-intensity, short-duration of rainfall, strain develops quite rapidly; however, at depth, the development is restricted because of the hindrance caused by an ephemeral de-saturated zone. The evolution of plastic strain closely follows the pattern of horizontal displacement.

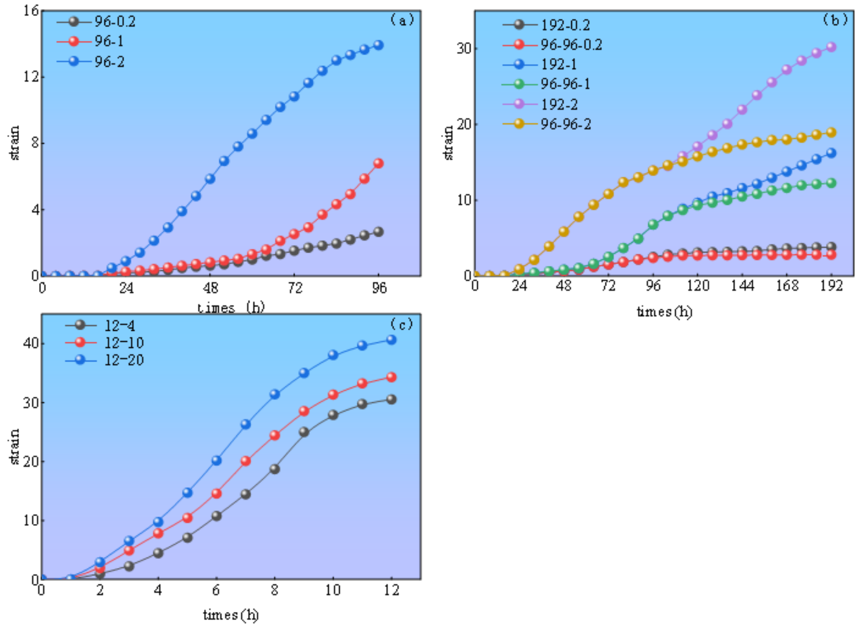

Figure 16. Equivalent plastic strain at the toe of the slope.

6. Discussion

6.1. Formation mechanism of the transient saturated zone and regional applicability

A distinct infiltration threshold was identified for the high-altitude gravelly soil slopes. This represents a saturated permeability coefficient of 1.9×10^{-4} cm/s (=6.84 mm/h). The infiltration above which stability is compromised is the infiltration threshold. When the intensity of rainfall is below this threshold, the infiltrating water can continue to percolate downwards. The surface layer (depth ≤ 0.5 m) will have a stable transient saturated zone within 2 h of exceeding the rainfall intensity threshold. This saturated zone has a function of barrier. Unlike the common case of silty clay slopes in low-altitude areas, a slope with high-altitude gravelly soil will, on the whole, have a larger saturated permeability coefficient. The above naturally gives rise to a higher critical rainfall intensity for appearance of a transient saturated zone. As such, early-warning thresholds for such slopes should be set differently as per field permeability tests.

6.2. Nonlinear evolution of the unsaturated permeability coefficient

The relative permeability coefficient and degree of saturation relationship play a critical role in defining the seepage behaviour of unsaturated soil. According to numerical simulations, when rainfall initially begins, for a low saturation degree when $S_r < 0.6$, the relative permeability coefficient k_r will be lower than 0.1 times the saturated value. As water continues to infiltrate, saturation will increase gradually up to 0.7–0.9 and k_r will also increase nonlinearly up to 0.3–0.8 times the saturated value. The cause of slope deformation's macro-characteristic "lagged initiation, accelerated development," is the internal "slow-to-fast" evolution of slope deformation.

6.3. Cumulative infiltration as a deformation early-warning indicator

Statistical relationships show that horizontal displacement at slope toe is significantly and positively correlated with cumulative infiltration. More specifically, for every 10 cm increase in cumulative infiltration, toe displacement increases by 15.2 mm ($R^2 = 0.93$, $p < 0.01$, 95% CI: 1.43–1.61). The physical ground for this relationship is that cumulative infiltration integrates the cumulative effect of total rainfall, rainfall intensity, and duration on the increase of water contents and decreasing of matric suction. We suggest an engineering early warning "dual indicator" system in which instantaneous rainfall intensity serves as the condition for issuing of a warning and cumulative infiltration serves as the condition for upgrading the warning.

6.4. Comparison with existing research and innovative contributions

The study on the slope stability of intrusions in the southeast Tibet region can be divided into three types. The first type estimates the rainfall threshold using statistical method. The second type utilizes a single-field finite element or finite difference analysis and cannot reveal the seepage-deformation coupling mechanism. The third group employs machine learning to evaluate susceptibility, but the input features are mostly static topographic factors.

This study makes clear innovative contributions in the following aspects:

1. The model incorporates parameter including the grain size distribution ($C_u = 38.2$, $C_c = 0.39$) and clay content (2.03%) of high-altitude gravelly soil.
2. Using Biot's fully coupled theory, the seepage field and deformation field are computed simultaneously, thus quantifying the whole-chain "infiltration pore pressure response displacement lag" process.
3. We determined a critical rainfall intensity (1.9×10^{-4} cm/s) for the transient state formation of the saturated zone and presented an empirical equation for cumulative infiltration-displacement.
4. Physical consistency in machine learning: We introduced physical constraint verification into the surrogate model.

6.5. Engineering significance

The engineering application value of this study is mainly reflected in the following aspects:

Identification of critical weak parts: the pore pressure response at the slope toe is detected 12 h earlier than at the slope crest, which makes the slope toe the most crucial area for drainage measures.

Through analyzing the double indicator relationship, the early warning zoning and grading are: the caution level (the rainfall intensity is >0.5 times K), the alert level (the rainfall intensity is >K), the warning level (the cumulative infiltration >5 cm, the displacement rate >2 mm/h), and the alarm level (the cumulative infiltration >10 cm and the displacement rate >5 mm/h).

Design optimization foundation: results show shallow reinforcement and surface drainage measures would be more appropriate than using deep anti-slide piles for such high-altitude gravelly soil slope protection measures.

6.6. Limitations and future work

The model utilized in this study does not account for seasonal freeze-thaw cycles, flow of snowmelt water and temperature gradients. Additionally, this study does not run gas–water two-phase flow simulation. Data from monitoring in the field are lacking at multiple depths. The Mohr-Coulomb constitutive model doesn't describe gravelly soil's behaviour during dilation or strain-softening. At a later stage, we will be able to establish a thermo-hydro-mechanical coupled model and integrate a physics-informed neural network (PINN) to enable stronger generalization of the surrogate model.

7. Conclusions

A distinct infiltration threshold exists for steep gravelly soil slopes. When the rainfall exceeds the amount of 1.9×10^{-4} cm/s, a temporary saturated zone is generated in the surface layer and a hydraulic barrier is formed. The deformation and plastic damage are concentrated in the shallow layer. The toe response of pore pressure and water content leads that of the crest by a considerable margin.

Cumulative infiltration is positively and significantly correlated with displacement and plastic strain. With an increase in cumulative infiltration by 10 cm, there is an increase in the toe displacement by 15.2 mm (R^2 = 0.93, 95% C.I: 1.43–1.61). After the rain ends, deformation lags by approximately 32 h.

The coefficient of relative permeability of high-altitude unsaturated coarse-grained soil changes nonlinearly with the degree of saturation. The main factor that controls the evolution of seepage is gas-phase obstruction.

The triggering threshold of slope deformation caused by rainfall is determined by rainfall intensity; and the final extent of deformation caused by cumulative infiltration. Short-duration heavy rainfalls ($I > K$) mainly cause shallow failure, while long-duration low to moderate rainfalls ($I < K$) generally cause deep progressive instability.

The constructed random forest surrogate model appears also able to reproduce the finite element calculation results with a high degree of fidelity (displacement R^2 = 0.964, RMSE = 1.27 mm; pore pressure R^2 = 0.971, RMSE = 2.54 kPa). The prediction time for each sample is below 0.1 s, with a speedup ratio that exceeds 50,000. The classification model is able to distinguish the transient saturated zone with 92.3% accuracy. The study results can provide model support to quickly give warnings about the rainfall-induced disasters on steep and high slopes of the Sichuan-Tibet highway.

Author contributions: Conceptualization, JJ and YZ (Yuhao Zheng); methodology, JJ and YZ (Yuhao Zheng); software, YZ (Yuhao Zheng) and YZ (Yongchen Zong);

validation, BW and QH; formal analysis, YZ (Yuhao Zheng); investigation, YZ (Yongchen Zong); resources, JJ; data curation, YZ (Yuhao Zheng); writing—original draft preparation, YZ (Yuhao Zheng); writing—review and editing, JJ and QH; visualization, YZ (Yuhao Zheng); supervision, JJ; project administration, JJ; funding acquisition, JJ. All authors have read and agreed to the published version of the manuscript.

Funding: This work was supported by the open project fund of the key laboratory of bridge structure wind resistance technology in the transportation industry (KLWRTBMC21-01).

Institutional review board statement: Not applicable.

Informed consent statement: Not applicable.

Data availability statement: The data presented in this study are available on request from the corresponding author. The data are not publicly available due to privacy restrictions.

Conflict of interest: The authors declare no conflict of interest.

AI use statement: During the preparation of this manuscript, the authors used ChatGPT solely for language refinement. No AI tools were used for data analysis, interpretation, or generation of scientific content. All outputs were critically reviewed and edited by the authors. The authors take full responsibility for the integrity and accuracy of the work.

References

1. Nury AH, Sharma A, Mehrotra R, et al. Projected changes in the Tibetan Plateau snowpack resulting from rising global temperatures. Journal of Geophysical Research: Atmospheres. 2022; 127(6): e2021JD036201. doi: 10.1029/2021JD036201
2. Sun Y, Liu S, Liu Y, et al. Effects of the interaction among climate, terrain and human activities on biodiversity on the Qinghai–Tibet Plateau. Science of the Total Environment. 2021; 794: 148497. doi: 10.1016/j.scitotenv.2021.148497
3. Tian P, Lu H, Feng W, et al. Large decrease in streamflow and sediment load of Qinghai–Tibetan Plateau driven by future climate change: A case study in Lhasa River Basin. Catena. 2020; 187: 104340. doi: 10.1016/j.catena.2019.104340
4. Tang L, Duan X, Kong F, et al. Influences of climate change on area variation of Qinghai Lake on Qinghai–Tibetan Plateau since 1980s. Scientific Reports. 2018; 8(1): 7331. doi: 10.1038/s41598-018-25683-3
5. Kunwar RM, Subedi BP, Baral SR, et al. Ethnobotany of the Himalayas: The Nepal, Bhutanese, and Tibetan Himalayas. In: Kunwar RM, Sher H, Bussmann RW (editors). Ethnobotany of the Himalayas. Springer; 2021. pp. 65–103. doi: 10.1007/978-3-030-57408-6_5
6. Yao M, Shao D, Lv C, et al. Evaluation of arable land suitability based on the suitability function—A case study of the Qinghai–Tibet Plateau. Science of the Total Environment. 2021; 787: 147414. doi: 10.1016/j.scitotenv.2021.147414
7. Zhou MD, Lü TY, Zhang YS, et al. The geological structure background and the crustal structure in the northeastern margin of the Qinghai–Tibetan Plateau. Acta Seismologica Sinica. 2000; 13(6): 687–697. doi: 10.1007/s11589-000-0071-2
8. Pan G, Wang L, Li R, et al. Tectonic evolution of the Qinghai–Tibet Plateau. Journal of Asian Earth Sciences. 2012; 53: 3–14. doi: 10.1016/j.jseaes.2011.12.018
9. Wang F, Xu P, Wang C, et al. Application of a GIS-based slope unit method for landslide susceptibility mapping along the Longzi River, southeastern Tibetan Plateau, China. ISPRS International Journal of Geo-Information. 2017;

6(6): 172. doi: 10.3390/ijgi6060172

10. Wu GQ, Xie YL, Wei J, et al. Water migration in subgrade soil under seasonal freeze–thaw cycles in an alpine meadow on the Qinghai–Tibet Plateau. Journal of Mountain Science. 2022; 19(6): 1767–1781. doi: 10.1007/s11629-021-7270-9
11. Qu Y, Ni W, Niu F, et al. Shear properties and mechanism of freeze–thaw interface in unsaturated coarse-grained soil from Qinghai–Tibet Plateau. Advances in Civil Engineering. 2021; 2021(1): 6688724. doi: 10.1155/2021/6688724
12. Zhang YZ, Zhu XD, Liu WL, et al. Macro- and mesoscopic experimental study of the effects of water content on moisture migration in coarse-grained fillings under freeze–thaw cycles and loads. Cold Regions Science and Technology. 2022; 196: 103491. doi: 10.1016/j.coldregions.2022.103491
13. Zhang D, Li Q, Liu E, et al. Dynamic properties of frozen silty soils with different coarse-grained contents subjected to cyclic triaxial loading. Cold Regions Science and Technology. 2019; 157: 64–85. doi: 10.1016/j.coldregions.2018.09.010
14. Zhao M, Xie Q, Ren X, et al. Experimental research on the deformation and failure characteristics of coarse-grained soil slopes in seasonal frozen region along Sichuan–Tibet Railway. IOP Conference Series: Earth and Environmental Science. 2020; 455(1): 012135. doi: 10.1088/1755-1315/455/1/012135
15. Zhao W, Wang X, Xu Z, et al. Experimental study on natural evolution characteristics of coarse-grained soil slope in seasonal frozen soil region. Journal of Engineering Geology. 2021; 29(5): 1497–1506. doi: 10.13544/j.cnki.jeg.2020-174 (in Chinese)
16. Chen L, Mei L, Zeng B, et al. Failure probability assessment of landslides triggered by earthquakes and rainfall: A case study in Yadong County, Tibet, China. Scientific Reports. 2020; 10: 16531. doi: 10.1038/s41598-020-73727-4
17. Liu Y, Yao X, Gu Z, et al. Study of the automatic recognition of landslides by using InSAR images and the improved Mask R-CNN model in the Eastern Tibet Plateau. Remote Sensing. 2022; 14(14): 3362. doi: 10.3390/rs14143362
18. Gong Y, Yao A, Li Y, et al. Classification and distribution of large-scale high-position landslides in southeastern edge of the Qinghai–Tibet Plateau, China. Environmental Earth Sciences. 2022; 81(11): 311. doi: 10.1007/s12665-022-10433-6
19. Zeng Q, Yang Z, Shang Y, et al. Study on the bedrock-cover interface of the 102 landslide group on the Sichuan–Tibet Highway. Hydrogeology & Engineering Geology. 2008; 35(3): 1–6. (in Chinese)
20. Yuan G, Shang Y, Lin D. Engineering geological characteristics and stability evaluation of accumulation slopes in the Palongzangbu River Basin. Journal of Engineering Geology. 2009; 17(2): 188–194. (in Chinese)
21. Wei T. Stability and Rainfall Threshold Study of Typical Sandy Soil Slopes along the G318 Bolin Section [Master's Thesis]. Tibet University; 2022. (in Chinese)
22. Li J, Wang C, Wang G, et al. Analysis of influencing factors and coupling strength of landslide development based on quantitative theory III. Chinese Journal of Rock Mechanics and Engineering. 2010; 29(6): 1206–1213. (in Chinese)
23. Mei G. Review of slope stability analysis methods: From deterministic analysis to intelligent prediction. Journal of Engineering Research and Reports. 2026; 28(3): 189–197. doi: 10.9734/jerr/2026/v28i31830
24. Ghimire S, Guéguen P, Giffard-Roisin S, et al. Testing machine learning models for seismic damage prediction at a regional scale using building-damage dataset compiled after the 2015 Gorkha Nepal earthquake. Earthquake Spectra. 2022; 38(4): 2970–2993. doi: 10.1177/87552930221106495
25. Liu Y, Gong B, Su H. Study on soil-water characteristic curves of unsaturated soils. Geotechnical Investigation & Surveying. 2002; 30(3): 8–11. Available online: https://kns.cnki.net/kcms2/article/abstract?v=jXpGf_Tis3C-DFH2MQF6A9auVqmL5UQ_GTcDKB0R0yecvW2cSL1JEH4rvggHbFAW0J5M9ysX-pLIvHHZiS-291_ohDKiLE-jrkf7VGP4OhtDHE6srsXah4pL_gWTFati9z5J9krogXOb8HPZPcfmvwEbLCYiXiio&uniplatform=NZKPT (in Chinese)
26. Ahmad H, Zhang Y, Alam M, et al. An efficient reliability assessment of coupled FDM-DEM slope stability using physics-informed feature-based surrogate machine learning techniques. Computers and Geotechnics. 2026; 196: 108185. doi: 10.1016/j.compgeo.2026.108185